Title: Shape analysis of gamma rhythm supports a superlinear inhibitory regime in an inhibition-stabilized network

Running title: Shape analysis of gamma rhythm

Authors: R (first name) Krishnakumaran (last name)[1], Mohammed (first name) Raees (last name)[2] and Supratim (first name) Ray (last name)[1,2,*].

Affiliations:

[1]IISc Mathematics Initiative, Department of Mathematics, Indian Institute of Science, Bangalore, India, 560012

[2]Centre for Neuroscience, Indian Institute of Science, Bangalore, India, 560012,

Telephone +91 80 2293 3437, Facsimile +91 80 2360 3323

[*]**Corresponding Author:** sray@iisc.ac.in

Keywords: Gamma, Harmonics, Wilson-Cowan model, Phase analysis

Conflict of interest: The authors declare no competing financial interests.

Funding Disclosure: This work was supported by Wellcome Trust/DBT India Alliance (Senior fellowship IA/S/18/2/504003 to SR) and DBT-IISc Partnership Programme.

Acknowledgements: We thank Dr. Adam Kohn for his helpful comments on the paper.

Abstract

Visual inspection of stimulus-induced gamma oscillations (30-70 Hz) often reveals a non-sinusoidal shape. Such distortions are a hallmark of non-linear systems and are also observed in mean-field models of gamma oscillations. A thorough characterization of the shape of the gamma cycle can therefore provide additional constraints on the operating regime of such models. However, the gamma waveform has not been quantitatively characterized, partially because the first harmonic of gamma, which arises because of the non-sinusoidal nature of the signal, is typically weak and gets masked due to a broadband increase in power related to spiking. To address this, we recorded spikes and local field potential (LFP) from the primary visual cortex (V1) of two awake female macaques while presenting full-field gratings or iso-luminant chromatic hues that produced huge gamma oscillations with prominent peaks at harmonic frequencies in the power spectra. We found that gamma and its first harmonic always maintained a specific phase relationship, resulting in a distinctive shape with a sharp trough and a shallow peak. Interestingly, a Wilson-Cowan (WC) model operating in an inhibition stabilized mode could replicate the findings, but only when the inhibitory population operated in the super-linear regime, as predicted recently. However, another recently developed model of gamma that operates in a linear regime driven by stochastic noise failed to produce salient harmonics or the observed shape. Our results impose additional constraints on models that generate gamma oscillations and their operating regimes.

Significance Statement

Gamma rhythm is not sinusoidal. Understanding these distortions could provide clues about the cortical network that generates the rhythm. Here, we use harmonic phase analysis to describe these waveforms quantitatively, and show that the gamma rhythm in macaque V1, during the presentation of fullscreen plain-hues and achromatic-gratings, has a signature arch-shaped waveform, despite the variation in power and frequency reported earlier. We further demonstrate using population rate models that the non-sinusoidal waveform is dependent on the operating domain of the system generating it. Consequently, shape analysis provides additional constraints on cortical models and their operating regimes.

Introduction

Gamma rhythm refers to oscillatory neural activity in the 30-70 Hz range that changes in response to different stimuli and cognitive states (Buzsaki, 2006). In the primary visual cortex (V1), the gamma rhythm has been studied extensively using achromatic gratings, wherein gamma power and center-frequency have been shown to vary systematically with the properties of the grating (Jia et al., 2013; Murty et al., 2018). For instance, peak-frequency of gamma increases with the contrast of gratings (Ray and Maunsell, 2010; Jia et al., 2013) and, gamma power increases and frequency decreases with stimulus size (Gieselmann and Thiele, 2008; Ray and Maunsell, 2011). More recently, chromatic stimuli have also been explored, which, for low-wavelength (reddish) hues, can generate huge gamma oscillations that are an order of magnitude stronger than gamma produced by achromatic gratings (Shirhatti and Ray, 2018; Bartoli et al., 2019; Peter et al., 2019).

Gamma oscillations are thought to reflect the push-pull activity of interconnected excitatory and inhibitory neurons, which has been demonstrated in different spiking network models (Tiesinga and Sejnowski, 2009; Mazzoni et al., 2015; Chariker et al., 2018; Keeley et al., 2019). However, since such large-scale network models have several parameters to be tuned and can become hard to interpret, simplified population rate models are often used. One pioneering model was proposed by Wilson and Cowan (WC; 1972), in which excitatory and inhibitory neurons were grouped into populations, and the dynamics of these populations were characterized. Variants of WC models have recently been used to explain some properties of the gamma rhythm. For example, based on the observation that gamma rhythm appears in short bursts and its phase does not vary linearly (Burns et al., 2010, 2011; Xing et al., 2012), a WC based model was proposed in which the activation function (input-output relationship) was linear but driven by Poisson noise (Kang et al., 2009; Xing et al., 2012). A variant of this model, in which an additional global excitatory population was added, was used to explain the stimulus

78 dependence of gamma oscillations (Jia et al., 2013). On the other hand, Jadi and Sejnowski
79 (2014) used a WC model with a non-linear (sigmoidal) activation function and showed that
80 constraining the model to operate in an inhibition stabilized mode (Tsodyks et al., 1997) and
81 the inhibitory population to operate in superlinear domain can also reproduce the size and
82 contrast dependence of gamma rhythm.

83 Although both these models can explain the stimulus dependence of gamma, the shape
84 of the rhythm likely depends on the presence (and type) of non-linearity. The shape could be
85 non-sinusoidal (see, for example, Figure 11 of Wilson and Cowan, 1972), which is represented
86 in the spectral domain as peaks at harmonics of the fundamental frequency. Such distortions
87 have been observed in various brain oscillations such as theta rhythm (for a review, see Cole
88 and Voytek (2017)). For gamma rhythm, a visual inspection of raw traces reveals some
89 distortion (Henrie and Shapley, 2005; Jia and Kohn, 2011; Jia et al., 2011; Ray and Maunsell,
90 2015), which is also corroborated by the presence of peaks at the first harmonic of the
91 fundamental gamma peak in the power spectra (Gieselmann and Thiele, 2008; Ray and
92 Maunsell, 2010; Shirhatti and Ray, 2018). However, a quantitative study of the gamma
93 waveform, which could potentially constrain the type and operating regime of models, has not
94 been undertaken. This is partly because the noise in the harmonic range could offset its phase
95 estimates if the harmonic is not prominent enough. To address this, we studied gamma
96 oscillations produced by presenting full-screen hues that generated salient gamma oscillations
97 with prominent harmonics (Shirhatti and Ray, 2018), characterized the shape, and tested
98 models that could replicate the shape.

99

Materials and Methods

Data Acquisition

We used LFP data recorded by Shirhatti and Ray (2018) from V1 of two female macaque subjects, whom we refer to as M1 and M2 (correspond to M1 and M3 in the earlier paper). Both monkeys were fitted with a titanium headpost and trained to perform a visual passive fixation task, after which a Utah array (96 and 81 electrodes for M1 and M2) was implanted in V1 (details of the surgery and implants are provided in Shirhatti and Ray (2018)). The raw signals from microelectrodes were recorded using the 128-channel Cerebus neural signal processor (Blackrock Microsystems). LFP was obtained by filtering the raw signals online between 0.3 Hz and 500 Hz (Butterworth filters; first-order analog and fourth-order digital respectively), and recorded at 2 kHz sampling rate and 16-bit resolution. No further offline filtering was performed on this data before analysis.

Multiunit activity was also extracted from the raw signal by filtering online between 250 Hz and 7.5 kHz (Butterworth filters; fourth-order digital and third-order analog respectively), and subjecting the resultant signal to an amplitude threshold of ~5 SD of the signal. The recorded units were found to have receptive fields located in the lower left quadrant of the visual field with respect to fixation in both monkeys, at an eccentricity of ~3°–4.5° in M1 and ~3.5°– 4.5° in M2. Full-field iso-luminant hues did not drive the neurons well, and therefore we did not get usable spiking activity from most electrodes. Therefore, as in our previous report (Shirhatti and Ray, 2018), all the analyses were performed only using LFP data (see Supplementary Figure 1 of Shirhatti and Ray, 2018, for description of spiking activity).

Experimental setup and behavior

During the experiment, the monkey was seated in a monkey chair with its head held stationary by the headpost. The monkey viewed a monitor (BenQ XL2411, LCD, 1,280 × 720 resolution, 100 Hz refresh rate) placed ~50 cm from its eyes. The monkey and the display setup

were housed in a Faraday enclosure with a dedicated grounding separate from the main supply ground to provide isolation from external electrical noise. The monitor was calibrated and gamma-corrected using i1Display Pro (x-rite PANTONE) to obtain a mean luminance of 60 cd/m^2 on its surface and to obtain a gamma of unity for each of the three primaries of the color gamut, which had the following CIE chromaticity xy coordinates: red, (0.644, 0.331); green, (0.327, 0.607); blue, (0.160, 0.062). The white point was at (0.345, 0.358).

Each monkey performed a passive fixation task, which required them to fixate at a small dot of 0.05°–0.10° radius at the center of the screen throughout the trial (3.3 or 4.8 s duration; fixation spot was displayed throughout). Each trial began with fixation, following which an initial blank grey screen of 1,000 ms was displayed, and then, two to three stimuli were shown for 800 ms each with an interstimulus interval of 700 ms. The monkey was rewarded with juice for maintaining fixation within 2° from the fixation point. Trials in which fixation was broken were not considered in our analyses. Eye position data was recorded as horizontal and vertical coordinates using the ETL-200 Primate Eye Tracking System (ISCAN) and monitored throughout the task using custom software running on macOS, which also controlled the task flow, generated stimuli, and randomized stimuli presentation.

Stimuli

The stimuli consisted of 36 hues and 1 achromatic grating. The hues were equally spaced along the circular hue space of the standard HSV nomenclature (0° hue to 350° hue, where 0°, 120°, and 240° represent red, green, and blue respectively), which were displayed full screen and at full saturation and value. The achromatic grating was at an orientation of 90° and had a spatial frequency of 4 cpd for M1 and 2 cpd for M2. These grating parameters were optimized to capture strong fast gamma with minimal slow gamma (see Murty et al., 2018).

The full-screen stimuli, in our setup, subtended a visual angle of ~56° in the horizontal direction and ~33° in the vertical direction.

Electrode selection

As with our previous report (Shirhatti and Ray, 2018), electrodes were considered for analysis only if they gave consistent stimulus-induced changes and reliable receptive field estimates across sessions, determined by a receptive field mapping protocol that was run across multiple days (Dubey and Ray, 2019). Further, we discarded signals from electrodes with unusable or inconsistent signals, a high degree of crosstalk with other electrodes, or impedances outside the range of 250–2,500 KΩ for monkey M1 and 125–2,500 KΩ for M2. This resulted in 64 and 16 usable electrodes for M1 and M2, respectively.

Data Analysis

Stimulus presentations with excessive artifacts (<5.9% and <5.0% of presentations of each stimulus in M1 and M2) were discarded for each session, yielding 19.9±6.2 repeats in M1 and 20.2±1.0 repeats in M2 per stimulus.

Spectral analysis of LFP

For each stimulus, LFP recorded from -500 to 0 ms from stimulus onset was taken as the 'baseline period' and 250 to 750 ms from stimulus onset was taken as the 'stimulus period' to avoid the transient responses to the stimulus onset. This yielded a frequency resolution of 2 Hz in the Power Spectral Density (PSD). PSD was computed using the Multitaper method using the Chronux toolbox (Bokil et al., 2010), with three tapers. The change in power was calculated as 10 times the difference between base-10 logarithm of PSDs at stimulus period and baseline period, expressed in decibels (dB). Estimation of peak frequencies was done on these baseline-corrected PSDs.

Gamma range was taken as 30-70 Hz, and 'gamma peak frequency' was estimated as the highest peak within this range. In most stimulus conditions tested, a discernible 'second bump' was observed in the baseline-corrected PSD. The peak frequency of the second bump was estimated as the highest peak occurring beyond 12 Hz after the estimated gamma peak frequency up to 140 Hz, to exclude higher frequency bumps.

Analysis of gamma and harmonic phases

To compute the phase difference of gamma and its first harmonic, gamma and harmonic signals were extracted from LFP during the stimulus period by bandpass filtering using separate Butterworth filters (zero-phase; order 4). The passband for gamma was 20 Hz wide, centered around the gamma peak frequency, identified from trial-averaged PSD for a given stimulus and an electrode. The passband for the first harmonic of gamma was also 20 Hz wide but centered around twice the corresponding gamma peak frequency. The phases of these signals (φ_{gamma} and $\varphi_{harmonic}$) were then computed using Hilbert transform. The phase difference between gamma and its harmonic was calculated as:

$$\text{Phase difference} = |2*\varphi_{gamma} - \varphi_{harmonic}| \quad (1)$$

The above phase difference estimate was computed at each timepoint within the stimulus period of every trial for each electrode.

Effect of harmonic phase on gamma waveform

To illustrate the effect of the gamma-harmonic phase relationship on the shape of gamma waveform, gamma and its first harmonic were mimicked using sinusoids and the initial phase of gamma (φ_G) was varied. The formulation of gamma and harmonics were as follows:

$$\text{Gamma wave, } G = \cos(2\pi\ 45\ t + \varphi_G)$$

$$\text{Harmonic wave, } H = ¼* \cos(2\pi\ 90\ t)$$

194 Sum of gamma and harmonic = G + H (2)

195 These waveforms are displayed in Figure 4C along with the phase difference (Figure
196 4D) obtained by applying equation (1).

197 Experimental Design and Statistical Analysis

198 First, we tested our hypothesis that the second bump in PSD accompanying gamma was
199 indeed its harmonic by computing the ratio of harmonic to gamma peak-frequencies, obtained
200 from the trial-averaged change in power (dB) from baseline spectra for each electrode. The
201 ratios were subsequently subjected to a non-parametric Wilcoxon signed rank test (Null
202 hypothesis: median ratio = 2). The standard error (SE) of the median of the gamma-harmonic
203 frequency ratio was estimated by bootstrapping over N iterations (where N is the number of
204 datapoints). This involved random sampling with replacement of the ratio data N times and
205 estimating their median each time, which resulted in N medians, whose standard deviation (SD)
206 is reported as the standard error (SE).

207 Circular statistics on the gamma-harmonic phase difference data were computed in
208 Matlab using the Circular Statistics toolbox (Berens, 2009). The mean phase differences are
209 reported as MEAN ± CI in Figure 5, where MEAN is the circular mean and CI is the 95%
210 confidence interval of MEAN, under a Von Mises distribution (implemented in *circ_mean* and
211 *circ_confmean* functions of the Circular Statistics toolbox).

212 To validate that the distribution of gamma-harmonic phase differences was non-
213 uniform and, thus, assess the validity of circular mean estimates in Figure 5, we subjected trial-
214 averaged phase-differences gathered from all electrodes for a given stimulus to a Rayleigh test
215 of non-uniformity (Null hypothesis: uniform distribution of phases). When the gamma activity
216 recorded for a given stimulus has a specific waveform across electrodes, the corresponding

distribution of gamma-harmonic phase-differences will be unimodal. We considered this to be the case when the p-value of the Rayleigh test was less than 0.01.

Studying non-sinusoidal waveforms in mean-field models of gamma

To understand the factors resulting in the characteristic waveform of gamma, we investigated the gamma-harmonic phase relationship emerging in mean-field models introduced in earlier works, which produced gamma oscillations with power and frequency trends as observed in experiments. We explored the waveform in these models by identifying input regimes that produced a first-harmonic with a specific phase difference from the fundamental of gamma, as required for its arch-shape. We assessed the presence of such regimes in two models. The first model operated linearly and produced oscillations by virtue of stochastic time-varying inputs (Jia-Xing-Kohn or JXK model; Jia et al., 2013), while the second model had non-linear dynamics, which gave rise to gamma frequency limit cycles in response to constant inputs (Jadi and Sejnowski or JS model; Jadi and Sejnowski, 2014).

Jia-Xing-Kohn (JXK) model

Jia et al. (2013) defined a linear EI rate-model and extended it by adding a Global Excitatory Population (G) to approximate recurrent excitatory feedback within V1. The model, when subjected to step input, acts as a damped oscillator but produces oscillations by virtue of constant perturbation from the Poisson inputs. The original model, formulated in the paper, incorporates detailed stimulus descriptions, namely Masked Noise (MN) level and stimulus size (r). The stimulus size parameter (r) scales the extent of Network recurrence in steady-state proportionally as larger size stimuli excite a larger area of cortical cells, increasing the global feedback. In our simulations, the Masking Noise level (MN) has been set to 0, resulting in the following reduced formulation.

$$\tau_E \frac{dr_E}{dt} = -r_E + W_{EE}\lfloor r_E \rfloor - W_{EI}\lfloor r_I \rfloor + W_{EG}\lfloor r_G \rfloor + E_{inp}$$

$$\tau_I \frac{dr_I}{dt} = -r_I + W_{IE}\lfloor r_E \rfloor - W_{II}\lfloor r_I \rfloor + W_{IG}\lfloor r_G \rfloor + I_{inp}$$

$$\tau_G \frac{dr_G}{dt} = -r_G + r^2 . W_{GE}\lfloor r_E \rfloor$$

where $\lfloor x \rfloor = x \; if \; x > 0 \; and \; 0 \;\; otherwise,$ and E_{inp} and I_{inp} approximate a Poisson process with average rates IE and II respectively, which vary with stimulus contrast (c) as:

$$I_E = 40.\frac{c^2}{c^2 + 0.3^2};\; I_I = 32.\frac{c^2}{c^2 + 0.3^2} \qquad (3)$$

Parameter values of this model are given in Table 1.

Jadi-Sejnowski (JS) model

Jadi and Sejnowski (2014) used a simple rate model consisting of an excitatory and an inhibitory population with sigmoidal activation, operating as an Inhibition Stabilized Network (ISN) and constrained the input drives to the populations to reproduce the increase in power and decrease in peak frequency of gamma with increasing stimulus size as earlier studies have observed in V1 (Gieselmann and Thiele, 2008; Ray and Maunsell, 2011).

The model defines the population firing rates of Excitatory and Inhibitory populations as follows:

$$\tau_E \frac{dr_E}{dt} = -r_E + \sigma_E(W_{EE}r_E - W_{EI}r_I + I_E)$$

$$\tau_I \frac{dr_I}{dt} = -r_I + \sigma_I(W_{IE}r_I - W_{II}r_I + I_I)$$

$$\sigma_P(x) = \frac{1}{1+exp(\,m_P.(\theta_P - x)\,)} - \frac{1}{1+exp(m_P.\theta_P)} \qquad (4)$$

In this model, larger stimuli cause an increased inhibitory drive to the population, owing to suppression from the surrounding populations. Since the model operated close to a supercritical Hopf bifurcation, the amplitude and frequency of oscillations in firing rates could be closely

approximated by linearization of the model. The authors deduced and demonstrated that the model gave rise to the observed trends in the gamma when the inputs were such that the inhibitory population was strongly 'superlinear'. This means that the summed inputs to the inhibitory population (from recurrent and external sources; argument of σ_I in equation 4) must lie in a certain range of values where the activation function σ_I curves upwards (increasing in slope with increasing summed input). For the sigmoidal activation function used in equation 4, the summed inputs must operate in the lower half of the sigmoid. Superlinear activation of the excitatory population, on the other hand, was antagonistic (not strongly superlinear). The set of such inputs constitute the operating regime of the model, which we refer to as the 'superlinear' regime.

Identifying the operational input regimes using gamma-harmonic phase difference

Because the gamma-harmonic relationship was studied using LFP recordings in real data while the model simulations yielded firing rates of excitatory and inhibitory populations, these firing rates had to be converted to a 'proxy' LFP. The relationship between the two is complex (Hasenstaub et al., 2005; Einevoll et al., 2013; Mazzoni et al., 2015). For simplicity, we used the negative sum of population firing rates of the excitatory and inhibitory populations in the models as a proxy for LFP, since the LFP, being the extracellular potential, could be approximated to vary inversely with the depolarization (excitability) of these populations. We also approximated the LFP as the negative of just the excitatory or inhibitory populations, which yielded qualitatively similar results. We elaborate this further in the Discussion section.

The environment used for simulation was Matlab 2019b (Mathworks, RRID:SCR_001622), where the models were simulated by a forward Euler method, with parameters as in Table 1. Simulations were run for a duration of 2 seconds in time-steps of 0.1 ms, on all pairs of 41 excitatory and 41 inhibitory input values sampled from the ranges specified in Table 1. In each case, PSD of the LFP proxy was computed between 1-2 seconds

to avoid the initial slow transient. The gamma and harmonic peak frequencies were identified as frequencies containing maximum power in the 30-70 Hz range and twice the gamma peak frequency, respectively. For further analyses in the JS model, only those input combinations were considered for which gamma and harmonic frequency amplitudes were greater than 1e-3 and 1e-6 units respectively, to ensure phase analysis of oscillatory activity was not dominated by simulation errors or noise (grey region in Figure 7F). The LFP proxy signal was filtered using 20 Hz passbands centered at each frequency identified above. The gamma-harmonic phase difference (equation 1) was computed, just as for LFP in macaque data. An input point (pair of values supplied as excitatory and inhibitory input drives; stimulus parameters in the case of JXK) was said to be 'in-regime' if the gamma-harmonic phase difference was within 22.5 degrees from 180-degrees (ideal for arch shape; Figure 4).

Since JXK takes stochastic inputs, to assess if there is indeed a unique gamma-harmonic phase difference at each of the mean input-drive combinations tested and whether the model can indeed exhibit in-regime behavior, we ran the simulation 50 times (analogous to 50 different trials) for each stimulus condition. In each iteration, we considered the mean phase-difference over the 1-2 second interval. For every selected input combination, the mean phase difference over this interval in each iteration was taken and the resultant pool of 50 mean phase differences was subjected to Rayleigh test of uniformity to identify those inputs that have a 'consistent' gamma-harmonic phase relationship across iterations (p-value < 0.01). Among the qualifying input combinations, those input drive pairs for which the circular mean of mean phase differences across iterations lay within 180±22.5 degrees were deemed to be 'in-regime'. For JXK, the gamma-harmonic phase reported in Figure 6 is the circular average of the phase differences from all the iterations. The amplitudes of gamma and its first harmonic in the figure are estimated from the average PSD (examples in Figure 6C-D), computed as the mean of the PSDs obtained from 50 iterations for a given stimulus combination.

Results

We collected spikes and LFP from 96 and 81 electrodes from two monkeys, M1 and M2, while they viewed full-screen color patches of different hues. Limiting our analysis to electrodes with reliable estimates of RF centers (see "Electrode selection" section in Methods) yielded 64 and 16 electrodes from the two monkeys.

First harmonic of gamma oscillation

In Figure 1A-D, the top row shows the power spectral density (PSD; averaged across all trials and subsequently across all electrodes) of the LFP signal in subject M1 during baseline period (-500 to 0 ms from stimulus onset; black trace) and during stimulus period (250 to 750 ms from stimulus onset; color/grey trace; the color indicates the hue that was presented and grey trace represents gratings). The corresponding change in power (dB) from baseline (Figure 1A-D bottom row) shows a prominent peak in the gamma range, along with another prominent peak near twice the frequency. Figure 1E-H show the same plots from subject M2. We first tested whether this second peak was indeed at twice the frequency. For each electrode and stimulus, we measured the gamma peak frequency from trial-averaged baseline-corrected PSDs as the highest peak within the 30-70 Hz band, and the peak of the second bump as the highest peak occurring after 12 Hz past the identified gamma peak frequency but before 140 Hz (the identified peaks are highlighted by black crosses in Figure 1).

Figure 2 presents the medians of the frequency ratios of second bump to gamma peak frequencies for each stimulus (hues indicated by color, gratings by grey color), computed across all electrodes in each subject, with error bars indicating the standard error of the median computed by bootstrapping. The stimuli are arranged along the horizontal axis by the average gamma power across electrodes. The frequency ratios were tightly clustered around 2, especially for stimuli that produced strong gamma oscillations. To test whether the ratio for a given stimulus was significantly different from 2, the frequency ratios computed in different

electrodes for the stimulus were subject to a Wilcoxon signed rank test. Stimuli for which the ratios were found to be significantly different from 2 ($p < 0.01$) are indicated by open circles. Estimates of peak-frequency ratios for stimuli producing less gamma power were more susceptible to noise and showed larger deviations in frequency ratios. However, frequency ratios were distributed more narrowly around 2 for stimuli inducing stronger gamma. The median ratio value for M1 was 2.00±0.021, not significantly different from 2 ($p = 0.26$ for M1; Wilcoxon signed rank test). For M2, the median ratio was 1.95±0.026, significantly different from 2 ($p = 9.96e-6$; Wilcoxon signed rank test). However, note that because we computed PSDs over a 500 ms window, the frequency resolution was 2 Hz, which introduced some error in the estimated ratio. For example, if the true gamma and harmonic peaks are at 41 and 82 Hz, the estimated gamma will either be at 40 or 42 Hz, yielding a ratio of either 82/40 = 2.05 or 82/42 = 1.95. These margins of error are shown as dotted lines in Figure 2. Most of the points lay within these error margins, especially for electrodes with higher gamma power. When we restricted the analysis to the top ten hues for each monkey in terms of gamma power, the ratios were 1.98±0.046 ($p=1$; Wilcoxon signed rank test) and 1.99±0.014 ($p=0.38$; Wilcoxon signed rank test). These results confirm that the second peak was indeed the first harmonic of gamma. We also note that achromatic gratings failed to produce a salient harmonic in M2 (Figure 1H), yielding a ratio that was much less than 2 (Figure 2). Although the frequency ratios for achromatic gratings in most electrodes were concentrated near 1.5 (as indicated by the very small errorbars), a few electrodes (2 out of 16) gave ratios greater than 2, causing the Wilcoxon signed rank test to fail in rejecting the Null hypothesis (albeit with a small p-value of 0.042).

Shape of the gamma waveform

Figure 3 shows LFP traces from example trials corresponding to each stimulus case presented in Figure 1. These traces revealed a characteristic arch shape of gamma waveform, featuring narrower troughs separated by much broader crests, hinting at a characteristic

alignment of gamma fundamental and its harmonic in these cases (best observed in M2 when colored patches were shown).

To visualize how phase differences between gamma and its first harmonic components affected the shape of the summed signal, we added two sinusoids to emulate the fundamental and the first harmonic of gamma, at frequencies 45 Hz and 90 Hz respectively, and varied the initial phase of the 45Hz component (as described in equation 2; shown in Figure 4A). Figure 4B shows the waveforms produced at each of these phases, and Figure 4C indicates the corresponding values of our phase difference measure (computed as in equation 1) between gamma and its harmonic. Using our convention (equation 1), a phase difference of 180 degrees (Figure 4A-C row 3) gave the desired shape as troughs of both sinusoids aligned to produce a steeper overall trough.

Gamma waveform is similar in different hues

In Figure 5, we show the distribution of trial-averaged gamma-harmonic phase differences in all electrodes, for each stimulus (indicated by color), arranged horizontally in order of average gamma power produced. For each stimulus, the trial-averaged phase differences from all electrodes were subject to Rayleigh test, and the stimuli with non-uniform phase difference distributions (p-value < 0.01) are indicated by filled circles. The error bars in each case represent the 95% confidence interval of mean phase differences. The phase differences at higher gamma generating stimuli were distributed close to 180° in both subjects, as predicted from the arch-shaped waveforms (Figure 4). Stimuli that produced low power had high dispersion of phase differences, likely originating from higher influence of noise, as is visible from the larger confidence intervals in M1, resulting in some hues with nearly uniform phase difference distributions (unfilled circles; some cases lack error bars as confidence intervals could not be computed due to their near-uniform distributions). For hues that generated high gamma power, gamma-harmonic phase differences were concentrated slightly

386 higher than 180° for M1 and close to 180° for M2. The circular mean of electrode-averaged
387 phase difference between gamma and its first harmonic across those stimuli which showed
388 unimodal distribution (filled circles in Figure 5; 29 stimuli in M1 and all stimuli in M2) was
389 185.33±16.66 degrees for M1 (176.60±16.32 degrees if all stimuli were considered) and
390 153.90±5.56 degrees for M2. When restricted to the ten hues with the highest gamma power
391 for each monkey, the phases were 206.02±4.65 degrees for M1 and 170.23±3.00 degrees for
392 M2.

393 Gamma waveform in a linear population rate model with stochastic inputs

394 To test whether the stereotypical gamma waveforms observed in the data could be
395 modeled, we focused on two recently developed rate models by Jia, Xing and Kohn (2013;
396 abbreviated as the JXK model) and Jadi and Sejnowski (2014; JS model), both of which can
397 explain the contrast and size dependence of gamma oscillations (see Methods for details).

398 The JXK model, which is a piecewise linear model, operates as a damped oscillator in
399 its linear domain and produces sustained oscillations by virtue of time-varying input drives
400 generated by a Poisson process causing the responses to be stochastic as well. Hence, we
401 simulated the model over 2 seconds repeatedly for 50 iterations and analyzed the interval from
402 1-2 seconds ('analysis' window). Figure 6A shows the gamma peak amplitude obtained from
403 the average PSD of the LFP proxy across iterations for each stimulus size and contrast; Figure
404 6B shows the corresponding mean gamma peak frequencies. These plots show the model
405 replicating the stimulus size/contrast effects on gamma as demonstrated by Jia et al. (2013):
406 gamma frequency decreased and power increased as stimulus size increased, and gamma peak
407 frequency increased when contrast increased. Figure 6C shows the average PSD from all
408 iterations for different stimulus sizes (r) at a fixed contrast (c) of $10^{-0.25}$, showing a distinct
409 bump of activity in gamma range, whose peak frequency decreases but peak power increases
410 as we go from small to larger values of stimulus size (r). Likewise, Figure 6D shows the average

PSD for different contrasts and a fixed size of 4.375. The gamma peak frequency in the LFP proxy increased with contrast as demonstrated by Jia et al. (2013). However, the gamma bumps were broad, as expected of a noisy pseudoperiodic signal, and no prominent harmonic band activity was discernible in the PSDs. We performed phase analysis, considering the activity in the band centered around twice the gamma peak frequency (Figure 6B) as the harmonic band activity. Figure 6E shows the harmonic amplitudes and Figure 6F shows the mean gamma-harmonic phase differences of LFP proxy traces from different iterations. We searched for stimulus size and contrasts which yielded arch-shaped gamma, or equivalently a gamma-harmonic phase differences close to 180 degrees (Figure 4C, middle) consistently across iterations. Such domains of inputs are shown by black contours in Figure 6F and are identified as 'in-regime' stimuli (see Methods; *Identifying the operational input regimes using gamma-harmonic phase difference*). Such regimes were few and scattered sparsely. An example LFP proxy trace for the highest contrast condition in Figure 6D, which was in-regime, is shown in Figure 6G. The top panel shows the LFP proxy trace and the bottom panel shows the gamma (blue) and harmonic (red) band signals. The LFP traces exhibited bursts of gamma oscillations with randomly distorted waveforms, with no consistent relationship between gamma and the harmonic.

Gamma waveform in JS model

Jadi and Sejnowski (2014) simulated visually evoked gamma using a firing rate model with only an Excitatory and an Inhibitory population and demonstrated gamma as self-sustained oscillations in response to steady constant input drives. As a result, any waveform shape found in a cycle of the oscillations is repeated throughout. We studied whether this model could produce realistic gamma waveforms by identifying the input regime (pairs of input drives to Excitatory and Inhibitory population) that would give rise to gamma-harmonic phase difference around 180° in LFP.

We implemented the model with the parameters specified in Jadi and Sejnowski (2014) for different input drives as listed in Table 1, and computed the LFP proxy in each case. Figure 7A-B shows the gamma peak amplitude and frequency respectively computed from the LFP proxy for each input-combination. The region within the white contour indicates an inhibition-stabilized network in which the inhibitory inputs are superlinear (for details, see Jadi and Sejnowski (2014)). Figure 7C shows the PSDs of LFP proxies obtained for different inhibitory input drives and a constant excitatory drive (input-combinations marked by same colored markers in Figures 7A-B), simulating the variation of stimulus size at a fixed contrast, as simulated in Jadi and Sejnowski (2014). The PSDs demonstrate the decrease in peak frequency and increase in power of gamma in our LFP proxy signal with increasing stimulus size. To demonstrate the contrast effect, we chose a set of input-combinations where both excitatory and inhibitory input drives linearly increased with contrast (colored markers in Figures 7A-B). The PSDs of LFP proxy generated for increasing contrasts are shown in Figure 7D. The gamma frequency increased for higher contrasts mimicking gamma in LFP recordings (Jia et al., 2013). Importantly, this model showed prominent harmonics as well.

Figure 7F plots the gamma-harmonic phase differences in the LFP proxy trace generated for each input combination. Regions in the input drives where the phase difference fell within 22.5° from 180° are enclosed by contours (Figure 7F, black contours) and identified as ‘in-regime’. Interestingly, this identified regimes fell inside the region predicted by Jadi and Sejnowski, (2014) where inhibition was superlinear (Figure 7F, white contours), and hence both validated their earlier findings and constrained the model to operate in more restricted regions. Figure 7G presents an example LFP proxy trace in the top panel, corresponding to the largest size condition in Figure 7C (in-regime), whose gamma fundamental (blue) and first harmonic (red) components are shown in the bottom panel. The troughs of gamma and harmonic were indeed aligned, adding up to a wider crest and a sharper trough overall.

Figure 8 shows the gamma-harmonic phase differences and regimes found in both the models when the activity of only one population was taken as the LFP proxy. Figure 8A show the phase differences in the JXK model using -rE as LFP proxy and Figure 8B shows the results using -rI. As before, no connected region of in-regime stimuli could be found (similar to the case in Figure 6F). Figure 8C-D show the phase differences found in the JS model using these LFP proxies. While the location and number of in-regime inputs identified were different, the superlinear regime was still found to contain a connected region of in-regime inputs in either case. This suggests that an LFP proxy chosen as any non-negative linear combination of -rE and -rI, would give rise to 'in-regime' inputs within the superlinear regime of the JS model.

Discussion

We show quantitatively that gamma oscillations produced by different hues possess a distinctive arch-shaped waveform, which leads to a distinct peak at the first harmonic of gamma in the PSD, and a specific phase relationship between gamma and its harmonic. Further, we show that a linear, stochastically forced model proposed by Jia et al. (2013) does not produce distinct harmonics with consistent phase relationship and hence does not retain a specifically-shaped gamma waveform. On the other hand, a non-linear, self-oscillating model proposed by Jadi and Sejnowski (2014) produces prominent harmonics, and in a subdomain of inputs within the previously identified superlinear regime, the model generates the observed gamma waveform as well.

One important point to note is that this arch shaped gamma waveform with prominent harmonics were categorized for hue induced gamma, whereas most previous reports have used achromatic stimuli. In the achromatic stimulus used here, harmonics were not salient, especially for M2. However, although earlier experimental studies using achromatic gratings

485 did not describe or quantify the gamma waveform, visual inspection of raw LFP traces
486 containing gamma bursts reveal a similar shape in some studies (Jia and Kohn, 2011, Fig. 2;
487 Jia et al., 2011, Fig. 1A; Xing et al., 2012, Fig. 2; Brunet et al., 2014, Fig. 2D) showing that the
488 arch-shape of gamma is observed for at least some achromatic stimuli. The arch shape
489 described here is also visible when monkeys viewed colored natural images (Brunet et al.,
490 2015, Fig. 2). Interestingly, some papers (Gieselmann and Thiele, 2008, Fig. 1; Jia et al., 2011,
491 Fig. 9) have shown traces with an inverted arch shape. It is unclear why this is the case;
492 potential reasons could be due to differences in the position of the reference wire, cortical depth
493 of recording, or differences in the conductance level. For example, arch-shaped gamma
494 waveform is observed in biophysical ING-PING and spiking models as well (Mazzoni et al.,
495 2015, Fig. 4; Lowet et al., 2016, Fig. 4), in which non-sinusoidal gamma arises from the
496 dynamics of the voltage-gated conductances, and the specific shape produced by the model
497 varies when the conductances are varied. LFP waveform also changes with the recording depth
498 (Figure 4B versus 4C of Mazzoni et al., 2015). Non-sinusoidal waveforms are common in
499 neural rhythms, such as the sawtooth-shaped theta rhythm in the hippocampus and comb-
500 shaped beta rhythm, arising from a variety of different biophysical phenomena (Cole and
501 Voytek, 2017).

502 Gamma oscillations in the JXK model

503 JXK model, like another model proposed by Kang and colleagues (Kang et al., 2010),
504 explains the "bursty" nature of gamma oscillations, which was shown in previous studies
505 (Burns et al., 2010; Xing et al., 2012). These studies observed that gamma band power varied
506 during a trial, with short intervals (~130 ms) of high gamma power, interspersed by durations
507 of no prominent power. Based on these, Xing et al. (2012) suggested that gamma rhythms were
508 the outcome of cortical network resonating to the stochastic component in the inputs. During
509 periods in a trial when stochastic variations in input are less, the cortical network would tend

to asymptotically stabilize and oscillations would get weaker over time. Xing et al. (2012) demonstrated this mechanism in a piecewise linear asymptotically stable model with noisy inputs. The JXK model (Jia et al., 2013) emulated gamma burst-activity exhibiting the observed dependencies of gamma power and frequency on stimulus parameters such as size and contrast by varying input drives and recurrent excitation to the neural populations. However, the JXK model does not produce a consistent waveform shape, because despite the presence of a rectification component, the model operates mostly in a linear (post-rectification) domain for all inputs simulated. In this domain the step response would be sinusoidal oscillations damping exponentially over time. Although the presence of Poisson inputs distorted the waveform and prolonged oscillations for a longer duration, these distortions are not consistent across different cycles of oscillation. This was reflected as wide band of activity around the gamma band in the PSD (Figure 6C-D), and a lack of discernible harmonic activity. Therefore, while these models adequately explained the bursty nature of gamma oscillations, it is not surprising that they failed to produce a specific gamma waveform.

However, a recent study has shown that the duration of gamma 'burst' activity reported in Xing et al. (2012) could have been underestimated (Chandran KS et al., 2017). This error arises because the spectral estimator that is used to compute gamma power is itself noisy, causing the rhythm to appear bursty in the spectral domain (see Chandran KS et al. (2017) for details). Chandran KS et al. (2017) used Matching Pursuit algorithm with a Gabor dictionary, which chooses the best-matching template to estimate the duration of a gamma burst in the time domain itself to show that gamma bursts during presentation of achromatic grating were longer than reported earlier (median of ~300 ms, although the mode was ~100 ms). Along with the results presented here, this suggests that the gamma rhythm could have more temporal regularity than what is predicted by these stochastic models.

However, we note that the non-sinusoidal nature of gamma rhythm described here could be introduced in the JXK model by changing the activation function. Specifically, if a non-linear activation function is used in the place of the piece-wise linear rectifier, the step response of the system would itself be a specific non-sinusoidal waveform in subsequent cycles of the resulting damped oscillation. When stochastic perturbations are added, the resultant bursts of oscillatory activity will contain both irregular distortions caused by the noisily fluctuating inputs and more regular distortions induced by non-linearity at specific parts of the trajectory in each cycle. Therefore, although we show that our results are more consistent with JS instead of the JXK model, it is possible that the JXK model with a suitable activation function can also replicate our findings. Indeed, while the JS model generates the proper gamma shape within a sub-regime, the duration of gamma is as long as the duration of the stimulus itself. Therefore, some stochasticity may be necessary to replicate all features of gamma rhythmicity, including duration and shape.

In the JXK model, there were a few inputs that qualified our phase-difference criteria for 'in-regime' behavior. However, a close examination of the 'in-regime' trace (example in Figure 6G) revealed that, in addition to the irregularly distorted gamma cycles, these inputs had occasional isolated steep troughs. These steep troughs could be approximated by a negative impulse, which could be decomposed as a series of sinusoids with their troughs aligned, resulting in sporadic 180-degree phase-difference estimates. Since these distortions are of lower frequency than gamma, the JXK model does not operate 'in-regime' for any input combination.

Relationship between firing rates and LFP

JXK and JS models used excitatory cell activity to study the power and frequency trends of gamma. Here, we converted these firing rates to a "proxy" LFP to be compatible with the real data. Because the extracellular potential is generated due to the spatial separation of

559 transmembrane currents (generating dipoles or multi-poles), as well as alignment of such
560 dipoles across neurons, LFPs are thought to mainly reflect the transmembrane currents of
561 pyramidal neurons (Einevoll et al., 2013). But Hasenstaub et al. (2005), in their in-vivo study
562 of ferret prefrontal cortex, found that the postsynaptic potentials and the firing of regular-
563 spiking excitatory neurons and fast-spiking interneurons were both synchronized to the
564 extracellular gamma rhythm, but the activation of interneurons was more aligned with the
565 troughs of the oscillation. A modelling study (Mazzoni et al., 2015) simulated LFP using
566 various outputs of a Leaky Integrate-and-Fire (LIF) network (such as firing rates, membrane
567 potential and synaptic currents) and found that the sum of absolute values of synaptic currents
568 (with both AMPA and GABA currents weighted nearly equally) served as the best proxy for
569 LFP. As far as gamma oscillations are concerned, some studies have shown that spikes tend to
570 occur just before the trough of gamma (Chalk et al., 2010; Vinck et al., 2010; Das and Ray,
571 2018), with the pyramidal cells leading the interneurons by a few milliseconds (Csicsvari et
572 al., 2003; Hasenstaub et al., 2005; Vinck et al., 2013). In the JS model as well, we found that
573 the E population led the I population by about 50º or 2-3 ms in the superlinear regime. Further,
574 the results were qualitatively similar when just E or I or the sum of both were used as the LFP
575 proxy (Figure 7 and Figure 8).

576 Gamma and Harmonics vs slow/fast gamma

577 Murty et al., (2018) showed that fullscreen achromatic gratings produced two different
578 oscillations simultaneously – a fast gamma (40-70 Hz), which has been observed previously
579 for smaller sized gratings, and a slow gamma (20-40 Hz) which is prominent only for large
580 stimuli. Even though this also generates two bums in the PSD, fast gamma is not a harmonic
581 of the slow gamma. First, the center frequency of fast gamma was not twice that of slow
582 gamma. Second, slow and fast gamma were not co-tuned: they had distinct orientation,
583 contrast, temporal frequency and size tuning preferences.

584 The arch-shape shown here poses additional problems for phase coding schemes in
585 which spike position relative to the gamma phase is used to code information (Fries et al., 2007;
586 Vinck et al., 2010), because spikes tend to occur near the trough of the rhythm and having a
587 sharper trough reduces the operating range. Other studies have proposed that gamma
588 oscillations may not play a role but could be a useful marker/indicator of cortical processing
589 (Ray and Maunsell, 2015). In that framework, properties such as shape and duration along with
590 stimulus tuning could provide additional clues about the underlying circuitry.

591

592 References

593 Bartoli E, Bosking W, Chen Y, Li Y, Sheth SA, Beauchamp MS, Yoshor D, Foster BL
594 (2019) Functionally Distinct Gamma Range Activity Revealed by Stimulus Tuning in
595 Human Visual Cortex. Curr Biol 29:3345-3358.e7.

596 Berens P (2009) CircStat: A MATLAB Toolbox for Circular Statistics. J Stat Softw 31:1–21.

597 Bokil H, Andrews P, Kulkarni JE, Mehta S, Mitra PP (2010) Chronux: A platform for
598 analyzing neural signals. J Neurosci Methods 192:146–151.

599 Brunet N, Bosman CA, Roberts M, Oostenveld R, Womelsdorf T, De Weerd P, Fries P
600 (2015) Visual Cortical Gamma-Band Activity During Free Viewing of Natural
601 Images. Cereb Cortex 25:918–926.

602 Brunet NM, Bosman CA, Vinck M, Roberts M, Oostenveld R, Desimone R, De Weerd P,
603 Fries P (2014) Stimulus repetition modulates gamma-band synchronization in primate
604 visual cortex. Proc Natl Acad Sci U S A 111:3626–3631.

605 Burns SP, Xing D, Shapley RM (2011) Is Gamma-Band Activity in the Local Field Potential
606 of V1 Cortex a “Clock” or Filtered Noise? J Neurosci 31:9658–9664.

607 Burns SP, Xing D, Shelley MJ, Shapley RM (2010) Searching for autocoherence in the
608 cortical network with a time-frequency analysis of the local field potential. J Neurosci
609 Off J Soc Neurosci 30:4033–4047.

610 Buzsaki G (2006) Rhythms of the brain. Oxford University Press, USA.

611 Chalk M, Herrero JL, Gieselmann MA, Delicato LS, Gotthardt S, Thiele A (2010) Attention
612 reduces stimulus-driven gamma frequency oscillations and spike field coherence in
613 V1. Neuron 66:114–125.

614 Chandran KS S, Seelamantula CS, Ray S (2017) Duration analysis using matching pursuit
615 algorithm reveals longer bouts of gamma rhythm. J Neurophysiol 119:808–821.

616 Chariker L, Shapley R, Young L-S (2018) Rhythm and Synchrony in a Cortical Network
617 Model. J Neurosci 38:8621–8634.

618 Cole SR, Voytek B (2017) Brain Oscillations and the Importance of Waveform Shape.
619 Trends Cogn Sci 21:137–149.

620 Csicsvari J, Jamieson B, Wise KD, Buzsáki G (2003) Mechanisms of Gamma Oscillations in
621 the Hippocampus of the Behaving Rat. Neuron 37:311–322.

622 Das A, Ray S (2018) Effect of Stimulus Contrast and Visual Attention on Spike-Gamma
623 Phase Relationship in Macaque Primary Visual Cortex. Front Comput Neurosci 12
624 Available at: https://www.frontiersin.org/articles/10.3389/fncom.2018.00066/full
625 [Accessed March 15, 2019].

626 Einevoll GT, Kayser C, Logothetis NK, Panzeri S (2013) Modelling and analysis of local
627 field potentials for studying the function of cortical circuits. Nat Rev Neurosci
628 14:770–785.

629 Fries P, Nikolić D, Singer W (2007) The gamma cycle. Trends Neurosci 30:309–316.

630 Gieselmann MA, Thiele A (2008) Comparison of spatial integration and surround
631 suppression characteristics in spiking activity and the local field potential in macaque
632 V1. Eur J Neurosci 28:447–459.

633 Hasenstaub A, Shu Y, Haider B, Kraushaar U, Duque A, McCormick DA (2005) Inhibitory
634 Postsynaptic Potentials Carry Synchronized Frequency Information in Active Cortical
635 Networks. Neuron 47:423–435.

636 Henrie JA, Shapley R (2005) LFP Power Spectra in V1 Cortex: The Graded Effect of
637 Stimulus Contrast. J Neurophysiol 94:479–490.

638 Jadi MP, Sejnowski TJ (2014) Regulating Cortical Oscillations in an Inhibition-Stabilized
639 Network. Proc IEEE Inst Electr Electron Eng 102.

640 Jia X, Kohn A (2011) Gamma rhythms in the brain. PLoS Biol 9:e1001045.

641 Jia X, Smith MA, Kohn A (2011) Stimulus Selectivity and Spatial Coherence of Gamma
642 Components of the Local Field Potential. J Neurosci 31:9390–9403.

643 Jia X, Xing D, Kohn A (2013) No consistent relationship between gamma power and peak
644 frequency in macaque primary visual cortex. J Neurosci Off J Soc Neurosci 33:17–25.

645 Kang K, Shelley M, Henrie JA, Shapley R (2009) LFP spectral peaks in V1 cortex: network
646 resonance and cortico-cortical feedback. J Comput Neurosci Available at:
647 http://www.ncbi.nlm.nih.gov/entrez/query.fcgi?cmd=Retrieve&db=PubMed&dopt=Ci
648 tation&list_uids=19862612.

649 Kang K, Shelley M, Henrie JA, Shapley R (2010) LFP spectral peaks in V1 cortex: network
650 resonance and cortico-cortical feedback. J Comput Neurosci 29:495–507.

651 Keeley S, Byrne Á, Fenton A, Rinzel J (2019) Firing rate models for gamma oscillations. J
652 Neurophysiol 121:2181–2190.

653 Lowet E, Roberts MJ, Bonizzi P, Karel J, Weerd PD (2016) Quantifying Neural Oscillatory
654 Synchronization: A Comparison between Spectral Coherence and Phase-Locking
655 Value Approaches. PLOS ONE 11:e0146443.

656 Mazzoni A, Lindén H, Cuntz H, Lansner A, Panzeri S, Einevoll GT (2015) Computing the
657 Local Field Potential (LFP) from Integrate-and-Fire Network Models. PLOS Comput
658 Biol 11:e1004584.

659 Murty DVPS, Shirhatti V, Ravishankar P, Ray S (2018) Large Visual Stimuli Induce Two
660 Distinct Gamma Oscillations in Primate Visual Cortex. J Neurosci Off J Soc Neurosci
661 38:2730–2744.

662 Peter A, Uran C, Klon-Lipok J, Roese R, van Stijn S, Barnes W, Dowdall JR, Singer W, Fries
663 P, Vinck M (2019) Surface color and predictability determine contextual modulation
664 of V1 firing and gamma oscillations Colgin L, ed. eLife 8:e42101.

665 Ray S, Maunsell JH (2011) Different origins of gamma rhythm and high-gamma activity in
666 macaque visual cortex. PLoS Biol 9.

667 Ray S, Maunsell JHR (2010) Differences in Gamma Frequencies across Visual Cortex
668 Restrict Their Possible Use in Computation. Neuron 67:885–896.

669 Ray S, Maunsell JHR (2015) Do gamma oscillations play a role in cerebral cortex? Trends
670 Cogn Sci 19:78–85.

671 Shirhatti V, Ray S (2018) Long-wavelength (reddish) hues induce unusually large gamma
672 oscillations in the primate primary visual cortex. Proc Natl Acad Sci 115:4489–4494.

673 Tiesinga P, Sejnowski TJ (2009) Cortical enlightenment: are attentional gamma oscillations
674 driven by ING or PING? Neuron 63:727–732.

675 Tsodyks MV, Skaggs WE, Sejnowski TJ, McNaughton BL (1997) Paradoxical effects of
676 external modulation of inhibitory interneurons. J Neurosci Off J Soc Neurosci
677 17:4382–4388.

678 Veit J, Hakim R, Jadi MP, Sejnowski TJ, Adesnik H (2017) Cortical gamma band
679 synchronization through somatostatin interneurons. Nat Neurosci 20:951–959.

680 Vinck M, Lima B, Womelsdorf T, Oostenveld R, Singer W, Neuenschwander S, Fries P
681 (2010) Gamma-phase shifting in awake monkey visual cortex. J Neurosci Off J Soc
682 Neurosci 30:1250–1257.

683 Vinck M, Womelsdorf T, Buffalo EA, Desimone R, Fries P (2013) Attentional Modulation of
684 Cell-Class-Specific Gamma-Band Synchronization in Awake Monkey Area V4.
685 Neuron 80:1077–1089.

686 Wilson HR, Cowan JD (1972) Excitatory and inhibitory interactions in localized populations
687 of model neurons. Biophys J 12:1–24.

688 Xing D, Shen Y, Burns S, Yeh C-I, Shapley R, Li W (2012) Stochastic Generation of
689 Gamma-Band Activity in Primary Visual Cortex of Awake and Anesthetized
690 Monkeys. J Neurosci 32:13873–13880a.

691

692

Figures

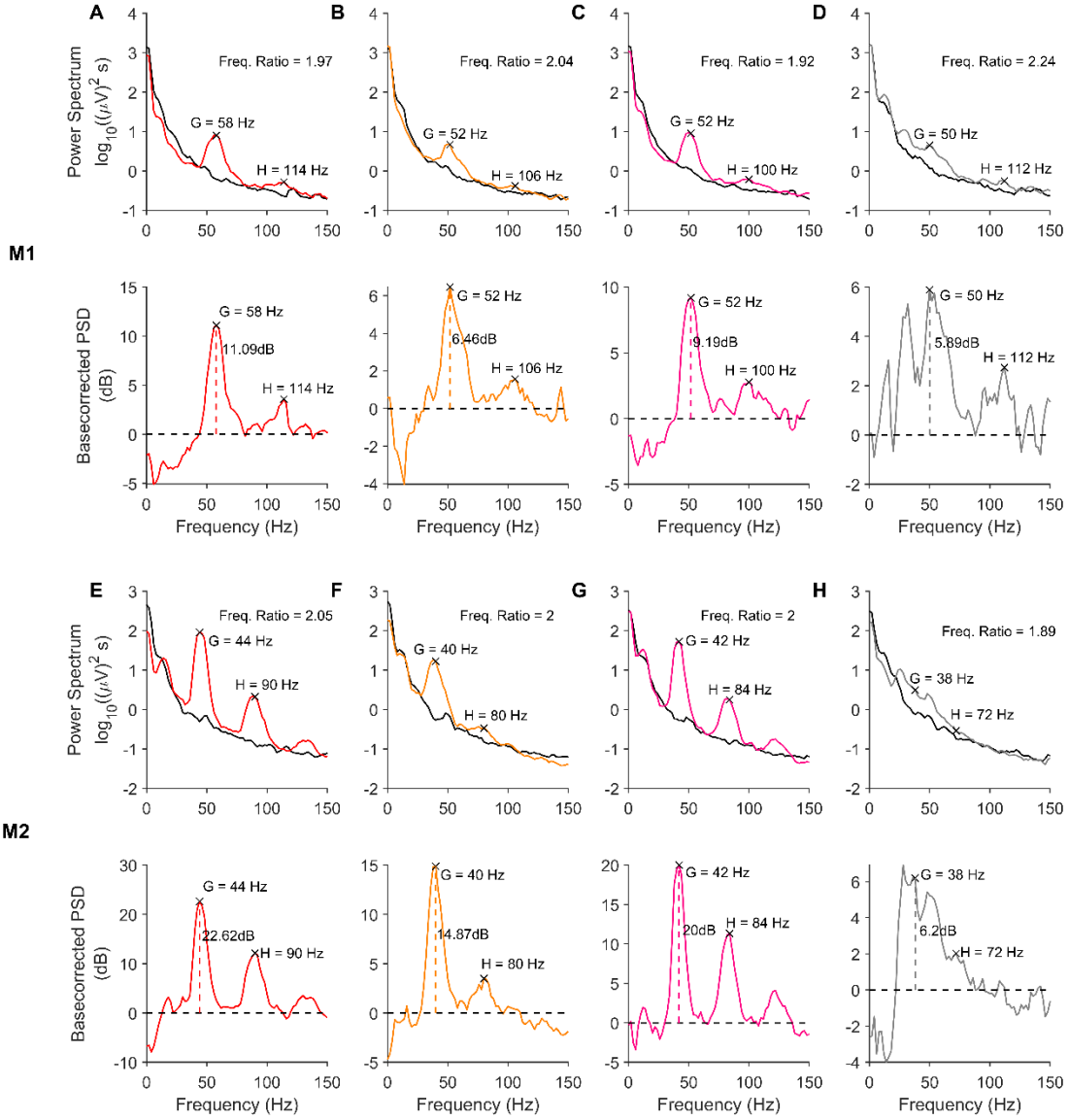

Figure 1: Visual Stimulation induces narrowband activity in gamma and its harmonic bands. (A-D, *top row*) PSDs for baseline (-500 to 0 ms; 0 indicates stimulus onset) and stimulus (250 to 750 ms) periods for different stimuli, averaged across trials and electrodes, from monkey 1 (M1). The baseline PSDs are plotted in black, while the stimulus period PSDs are colored (corresponding to the hue presented) or grey (for fullscreen grating). (A-D, *bottom row*) show the change in power (dB) in the stimulus period from the baseline, computed from the PSDs in the top row. The gamma power computed from the change in power spectrum is

represented by vertical dashed line). The peaks in gamma range and the second bump activity are marked in each plot. (E-H) Same as A-D, for monkey M2.

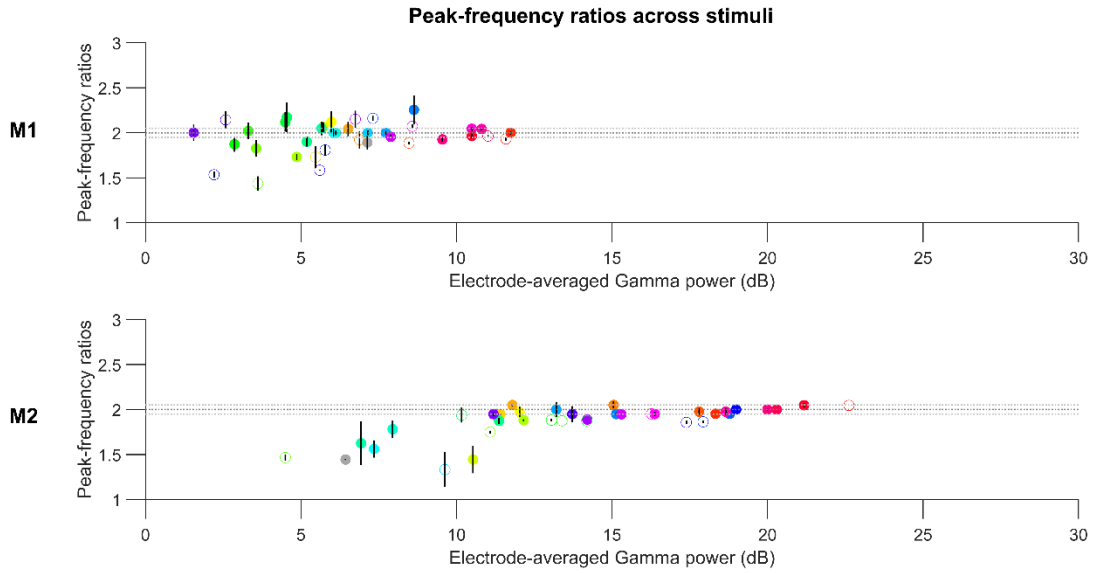

Figure 2: Second bump in PSD corresponds to the first harmonic of gamma. Median of peak frequency ratios of the second bump with respect to the gamma band, scattered against average gamma power for each stimulus (circles are colored to represent the presented hues; grating stimulus is represented by the grey circle). Error bars indicate the standard error of median (estimated by bootstrapping). Open circles mark stimuli whose ratios were found to be significantly different from 2 (p-value < 0.01 without any Bonferroni correction; Wilcoxon signed-rank test). The dotted horizontal lines correspond to the least-error margin 2±0.05.

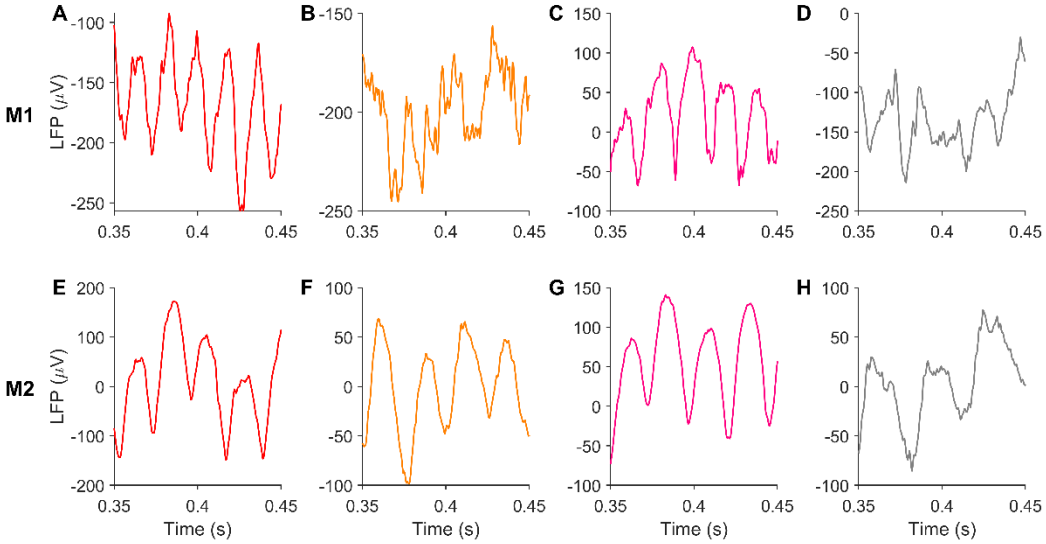

714

715 **Figure 3: Gamma waveform has consistent non-sinusoidal shape under different stimuli.**

716 (A-D) present LFP traces for different stimuli, shown in Figure 1, from an example trial and

717 electrode in M1. (E-H) shows LFP traces obtained from M2 for corresponding stimuli.

718

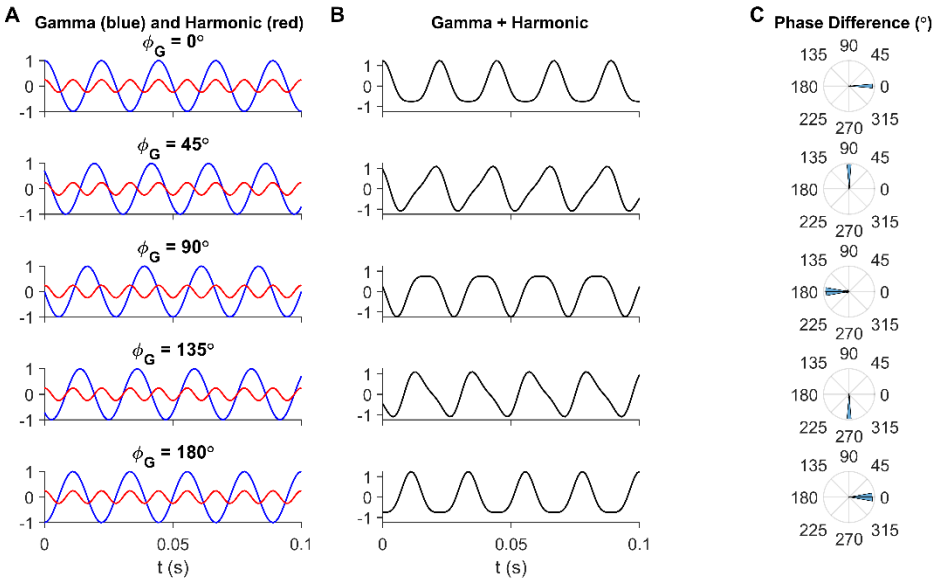

719

720 **Figure 4: Observed arch-shape of gamma corresponds to gamma-harmonic phase**
721 **difference of 180°.** (A) Gamma (blue) and harmonic (red) components, mimicked using
722 sinusoids as in equation (2) with different initial gamma phases (φ_G) in each row. (B) Gamma
723 waveform resulting from summation of gamma and its harmonic from the corresponding row
724 in (B). (C) Phase difference of gamma and its first harmonic, as given in equation (1), computed
725 from filtering and Hilbert transforming gamma and harmonic bands from the summed
726 waveform in (B) in each row. Note that the arch-shaped gamma observed in recordings arises
727 from a phase difference of 180° (middle row).

728

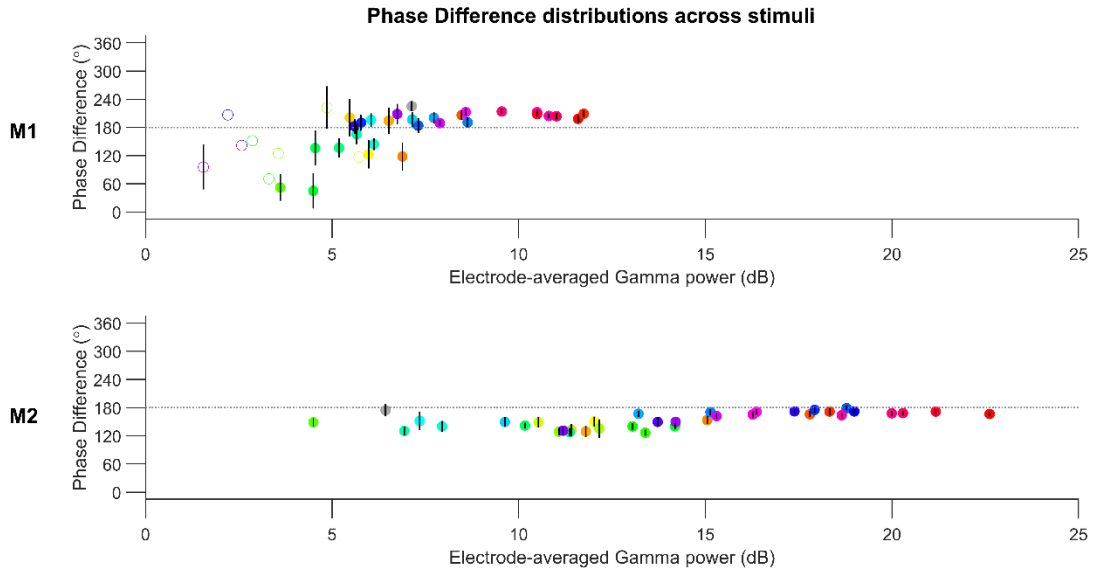

Figure 5: Gamma-harmonic phase differences in different stimuli are concentrated near 180°. Circular mean of trial-averaged gamma-harmonic phase differences (across all electrodes) are scattered against the average gamma power for each stimulus (circles are colored to represent the presented hues; grey for grating stimulus). For each stimulus, the pool of trial-averaged phase differences from all electrodes is subject to Rayleigh test of non-uniformity to check if phase-difference is consistent across electrodes so that circular mean estimates are reliable (p-value < 0.01). If found reliable (even though it could be different from 180º), the stimulus is represented by a filled circle. Error bars represent the 95% confidence interval of circular mean.

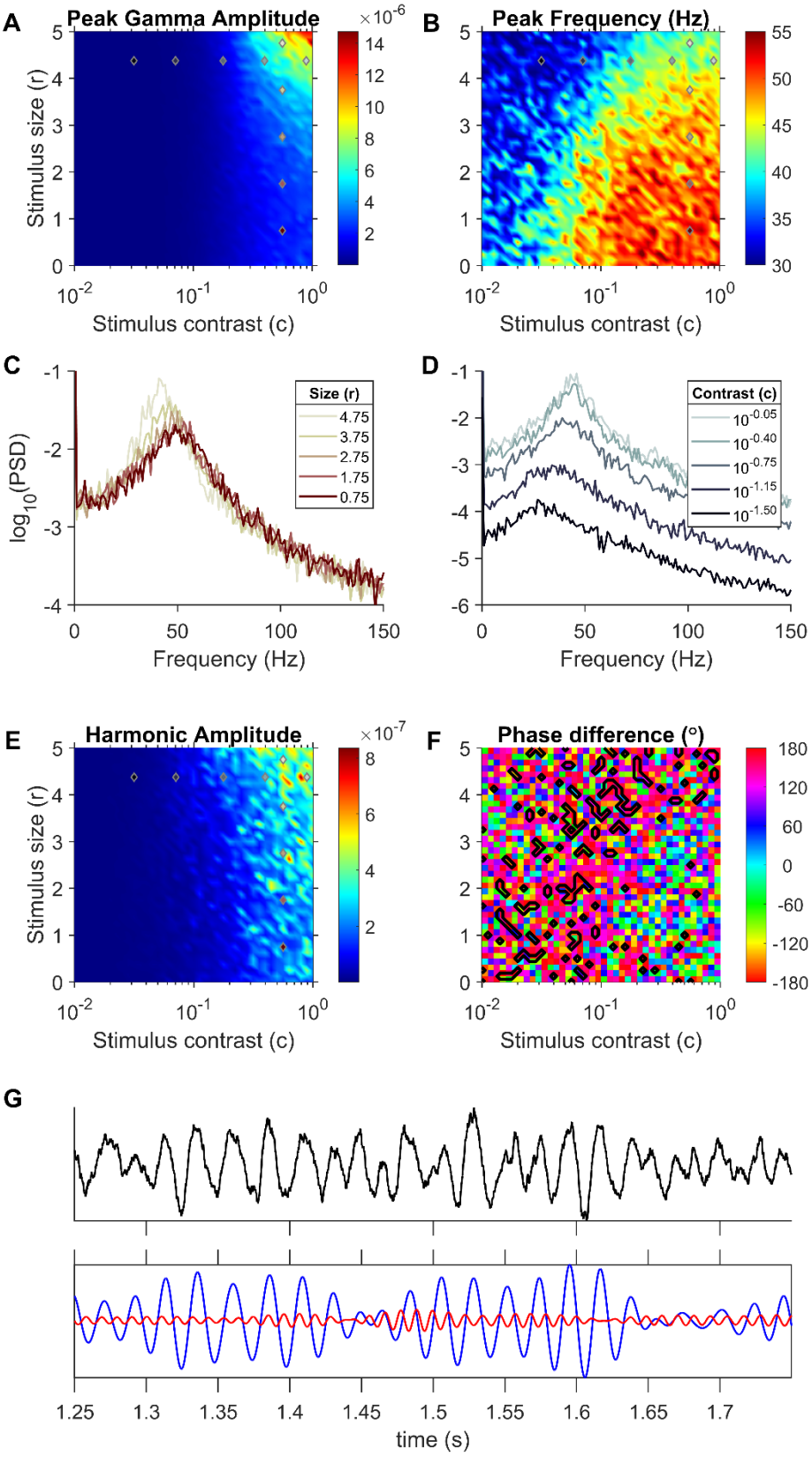

740

741 **Figure 6: Gamma properties for the JXK model** (A) Gamma peak amplitude and (B)
742 frequency found in the average PSD from 50 iterations at each stimulus size (r) and contrast
743 (c) combination. (C) Average PSD of LFP proxy traces generated at fixed contrast and different
744 sizes, across all iterations. (D) Average PSD of LFP proxy traces generated at different
745 contrasts at a fixed size. The stimuli values that generated these PSDs are indicated in plots
746 (A), (B) and (E) using colored markers (same colors as the plots in C and D). (E) Harmonic
747 band peak amplitude in the average PSD. The harmonic is taken to be twice of gamma
748 frequency. (F) Mean gamma-harmonic phase difference (equation (1)) across multiple
749 iterations, with in-regime inputs encircled by black contours. (G) Example LFP proxy activity
750 (top panel) and its gamma and first harmonic components (bottom panel) generated at the
751 highest contrast condition in (D) (identified as in-regime). This trace shows occasional steeper
752 troughs (bottom trace; near 1.35 s, 1.52 s and 1.58 s timepoints) although there is no consistent
753 trend between gamma and the harmonic.

754

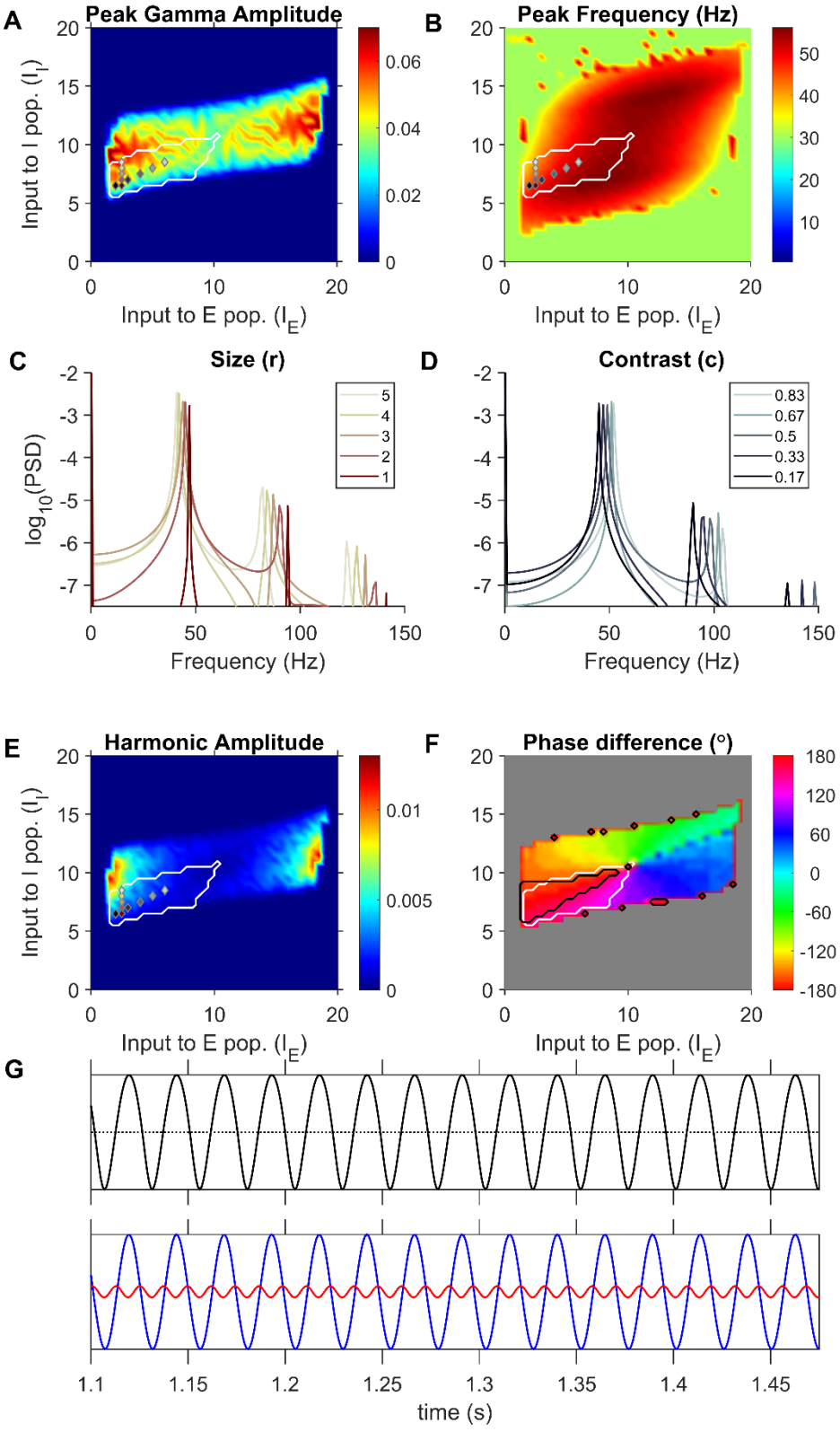

Figure 7: JS model produces sustained arch-shaped gamma oscillations within the previously identified superlinear inhibitory regime. (A) Peak gamma amplitude and (B)

Peak gamma frequency in the LFP proxy generated by the JS model for each input-drive combination. (C) PSD of LFP proxy generated for different stimulus sizes. (D) PSD of LFP proxy generated for different contrast. Input combinations used in (C) and (D) are indicated by markers, with same colors as traces, in (A), (B) and (E). (E) Harmonic amplitude identified from the PSD of LFP proxy for each stimulus condition. (F) Phase difference of gamma and its harmonic (equation (1)) computed for each simulated input drive pair. The black contours encircle input drives identified to be 'in-regime' from their phase differences. The white contour in each figure enclose the input domain identified by Jadi and Sejnowski (2014) to replicate gamma power increase and peak frequency decrease in response to increasing stimulus size, and it can be seen to enclose a significant portion of the 180° phase difference regime (black contour). (G) LFP proxy activity trace corresponding to the largest stimulus size shown in Figure 7C. The dotted horizontal line shown is equidistant from the minima and maxima of the traces. A sinusoidal oscillation would have the same crest and trough width on this line. The bottom panels show the gamma and its first-harmonic components, plotted in blue and red respectively, filtered from the LFP proxy traces.

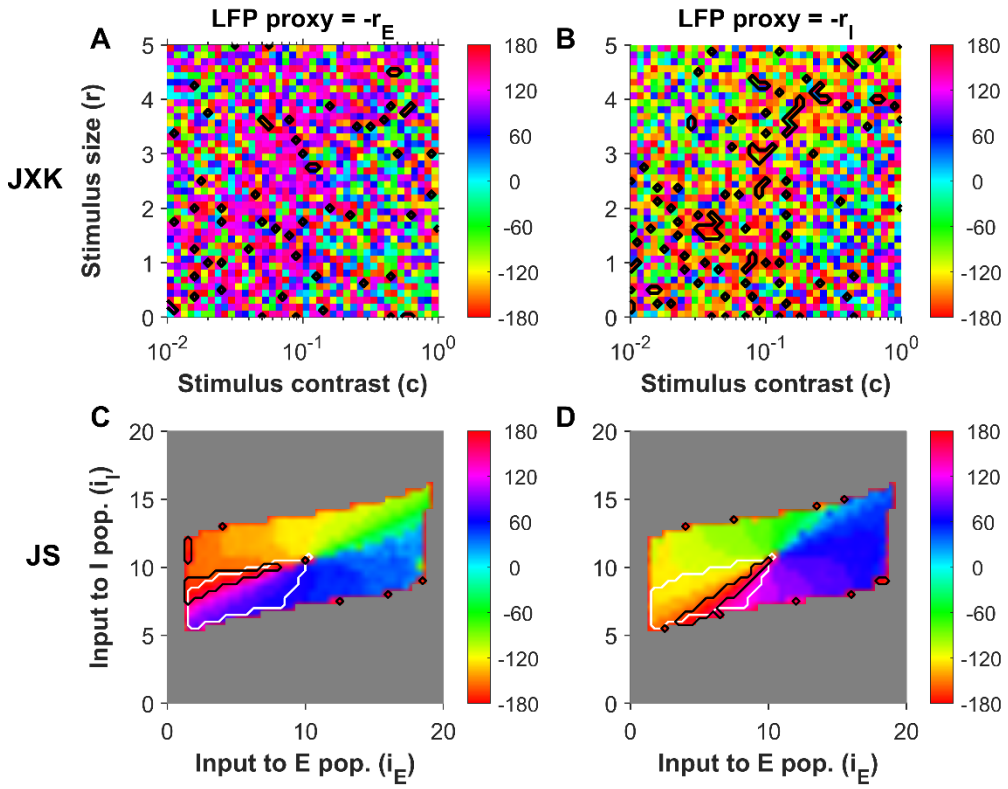

Figure 8: Gamma-harmonic phase difference in rate models using different LFP proxies. (A) Phase difference of gamma and its harmonic in the JXK model computed for each stimulus condition (as in Figure 6F) but using only E population activity to compute the LFP proxy. (B) Gamma-harmonic phase differences in JXK using I population activity alone. (C) Phase differences in JS model using E population activity only. (D) Phase differences in JS using I population activity only. Black contours encircle stimulus conditions identified as 'in-regime'. White contours in (C) and (D) mark the superlinear regime of the JS model.

783 Tables:

784 **Table 1: Parameter values used in rate models.**

JS							
W_{EE}	W_{EI}	W_{IE}	W_{II}	τ_E, τ_I (ms)			
16	26	20	1	20,10			
me,mi	thetae,thetai		I_E,I_I				
1,1	5,20	0 to 20 (steps of 2.5)					
JXK							
W_{EE}	W_{EI}	W_{IE}	W_{II}	W_{EG}	W_{IG}	W_{GE}	τ_E, τ_I, τ_G (ms)
1.5	3.25	3.5	2.5	0.25	0.5	0.6	6,15,19
MN	r		c				
0	1 to 5 (steps of 0.125)		0.01 to 1 (logarithmic steps of 0.5)				

785